



HAL
open science

An unfitted radial basis function generated finite difference method applied to thoracic diaphragm simulations

Igor Tominec, Pierre-Frédéric Villard, Elisabeth Larsson, Víctor Bayona,
Nicola Cacciani

► **To cite this version:**

Igor Tominec, Pierre-Frédéric Villard, Elisabeth Larsson, Víctor Bayona, Nicola Cacciani. An unfitted radial basis function generated finite difference method applied to thoracic diaphragm simulations. *Journal of Computational Physics*, 2022, pp.111496. 10.1016/j.jcp.2022.111496 . hal-03748102

HAL Id: hal-03748102

<https://inria.hal.science/hal-03748102v1>

Submitted on 9 Aug 2022

HAL is a multi-disciplinary open access archive for the deposit and dissemination of scientific research documents, whether they are published or not. The documents may come from teaching and research institutions in France or abroad, or from public or private research centers.

L'archive ouverte pluridisciplinaire **HAL**, est destinée au dépôt et à la diffusion de documents scientifiques de niveau recherche, publiés ou non, émanant des établissements d'enseignement et de recherche français ou étrangers, des laboratoires publics ou privés.

An unfitted radial basis function generated finite difference method applied to thoracic diaphragm simulations

Igor Tominec^a, Pierre-Frédéric Villard^b, Elisabeth Larsson^a, Víctor Bayona^c, Nicola Cacciani^{d,e}

^a*Uppsala University, Department of Information Technology, Division of Scientific Computing, Sweden*

^b*Université de Lorraine, CNRS, Inria, LORIA, Nancy, France*

^c*Departamento de Matemáticas, UC3M, Leganés 28911, Spain*

^d*Department of Physiology and Pharmacology, Karolinska Institutet, Stockholm, Sweden*

^e*Department of Clinical Neuroscience, Clinical Neurophysiology, Karolinska Institutet, Stockholm, Sweden*

Abstract

The thoracic diaphragm is the muscle that drives the respiratory cycle of a human being. Using a system of partial differential equations (PDEs) that models linear elasticity we compute displacements and stresses in a two-dimensional cross section of the diaphragm in its contracted state. The boundary data consists of a mix of displacement and traction conditions. If these are imposed as they are, and the conditions are not compatible, this leads to reduced smoothness of the solution. Therefore, the boundary data is first smoothed using the least-squares radial basis function generated finite difference (RBF-FD) framework. Then the boundary conditions are reformulated as a Robin boundary condition with smooth coefficients. The same framework is also used to approximate the boundary curve of the diaphragm cross section based on data obtained from a slice of a computed tomography (CT) scan. To solve the PDE we employ the unfitted least-squares RBF-FD method. This makes it easier to handle the geometry of the diaphragm, which is thin and non-convex. We show numerically that our solution converges with high-order towards a finite element solution evaluated on a fine grid. Through this simplified numerical model we also gain an insight into the challenges associated with the diaphragm geometry and the boundary conditions before approaching a more complex three-dimensional model.

Keywords: unfitted, RBF-FD, least-squares, elasticity, diaphragm, mixed boundary condition

1. Introduction

During the 2020 covid-19 pandemic we have all been made aware that intensive care units (ICU) have limited capacity with respect to the number of patients that can be cared for at the same time. The WHO report on covid-19 in China [1] indicates that covid-19 patients with severe symptoms need 3–6 weeks in ICU. Patients with severe respiratory symptoms are put under mechanical ventilation to save their lives. At the same time, the

URL: igor.tominec@it.uu.se (Igor Tominec), pierrefrederic.villard@loria.fr (Pierre-Frédéric Villard), elisabeth.larsson@it.uu.se (Elisabeth Larsson), vbayona@math.uc3m.es (Víctor Bayona), nicola.cacciani@ki.se (Nicola Cacciani)

7 mechanical ventilation has adverse effects, such as ventilator induced diaphragmatic dys-
8 function (VIDD) [2], which prolongs the ICU time. Hence, improving mechanical ventilation
9 can have a significant impact on ICU patient turnover.

10 This work is part of the INVIVE project¹, where we aim to create a mechanically venti-
11 lated virtual patient [3] on whom we can perform tests with different ventilation strategies
12 and counter measures against VIDD [4]. With the virtual patient, we can also vary the
13 gender, physiology, age and potential injuries that affect the response. Using simulations
14 allows to create a controlled computer-based environment in a way that is not possible in a
15 clinical setting.

16 The diaphragm is the main respiratory muscle, and the present focus of our study. The
17 diaphragm is located between the thoracic and abdominal cavities. It has two domes, and
18 is attached to the lower ribs, the spine, and the sternum. During mechanical ventilation,
19 the normal action of the diaphragm, where inhalation follows the contraction of the muscle,
20 is reversed, i.e., the muscles become passive and the air is pumped into the lungs by the
21 ventilator. As air is entering the lungs with a positive pressure, the muscle fibres are instead
22 extended. This sudden and extreme mechanical perturbation is the trigger of a chain of
23 biological events causing the progression of VIDD.

24 Numerical simulation of the biomechanical action of the diaphragm during respiration
25 or ventilation is a challenging problem. The shape of the diaphragm is non-trivial and there
26 are gradual transitions between muscle and tendon with very different material response.
27 Imperfect data can be extracted from medical images, and can then be converted into a
28 geometry representation [5]. The specific challenges of constructing a smooth geometry
29 representation are addressed in a forthcoming paper [6].

30 In this paper, we model the diaphragm using a linear elastic PDE. This is a simplification
31 and we plan to develop a more realistic tissue model as a part of our future work.

32 The boundary conditions for the elastic PDE system are given by a combination of trac-
33 tion boundary conditions, which contains first derivatives of the displacement, and (time-
34 dependent) Dirichlet boundary conditions for the displacement, where the diaphragm is
35 attached. These are mixed boundary conditions, in general not fully compatible, leading to
36 reduced regularity of the solution even when we expect a smooth solution from a physiolog-
37 ical perspective. Therefore, we smooth the boundary data as well as the transition between
38 the traction boundary data and Dirichlet boundary data before using it in the PDE solver.

39 We use the unfitted radial basis function generated finite difference method in the least-
40 squares setting (unfitted RBF-FD-LS) [7] to solve the diaphragm problem. A benefit of using
41 the unfitted RBF-FD-LS method is that the PDE problem is solved on an extended domain
42 (see Figure 3). This simplifies node generation as the node placement is then independent of
43 the geometry. Another benefit of the unfitted setting is a smaller approximation error near
44 the boundaries [7], where the stencils are typically highly skewed when using conventional
45 RBF-FD methods such as the fitted RBF-FD-LS method [8] and the collocation RBF-FD
46 method [9].

47 As model geometry we use a two-dimensional cross section of the diaphragm. To inves-
48 tigate the properties of the problem we use a combination of data from medical images and
49 knowledge about the physiology of the diaphragm expressed in terms of boundary condi-
50 tions. In particular, we construct two benchmark problems: (i) a pure Dirichlet case, (ii) a
51 case with mixed boundary conditions (Dirichlet + traction), rephrased as a Robin condition

¹https://www.it.uu.se/research/scientific_computing/project/rbf/biomech

52 with smooth coefficients. With the experiments performed for these benchmarks, we aim to
53 answer the following questions:

- 54 • Can we solve the benchmarks problems with unfitted RBF-FD-LS? Are there specific
55 numerical challenges to be noted?
- 56 • Can we achieve high-order convergence to the solution of the elastic PDE when the
57 imposed boundary data and the geometry is smooth?
- 58 • How is the performance and accuracy of the RBF-FD-LS solver affected by the type
59 of boundary conditions that are imposed?
- 60 • How does the RBF-FD-LS solver compare with a basic FEM solver? Do the solvers
61 give similar solutions?

62 Other authors have also modeled the diaphragm numerically. The most advanced di-
63aphragm simulations in the literature can be found in a series of publications by Ladjal
64 et al. [10, 11, 12, 13, 14]. The application focus is to track the motion of lung tumours
65 during respiration for radiotherapy purposes. The finite element models that are employed
66 are highly elaborate, taking into account features such as patient-specific lung compliance
67 in order to define the constitutive law. The simulation times reported are far from real-time
68 capability. In these studies, the diaphragm is not the main target and it is not well-resolved
69 in the thickness direction due to the high aspect ratio. Other relevant, but less detailed,
70 diaphragm simulations can be found in [15], where the diaphragm is discretized using shell
71 elements to compare healthy and pathological situations, and in [16], where the whole region
72 under the lungs, including the diaphragm, forms one region in the simulation.

73 The outline of the paper is as follows: Section 2 describes the expected behavior of the
74 diaphragm during respiration and the relation of the two-dimensional geometry to the real
75 three-dimensional diaphragm geometry. Then the linear elasticity model problem is defined
76 in Section 3. An RBF-FD algorithm for computing differentiation and evaluation matrices
77 is described in Section 4. In Section 5 these matrices are then used in the least-squares un-
78 fitted RBF-FD setting to discretize the linear elasticity equations. Section 6 discusses how
79 the boundary of the two-dimensional diaphragm cross-section, and the boundary conditions,
80 are smoothed. In Section 7 and Section 8 we compute the solution to the linear elastic-
81 ity equations for the two benchmark problems, and evaluate the convergence numerically.
82 Finally, Section 9 contains the conclusions.

83 2. The expected behavior of the thoracic diaphragm

84 The diaphragm is a musculotendinous structure, approximately double-dome shaped,
85 separating the thoracic and abdominal cavities. It is the main muscle of the physiological
86 respiration, performing 70–80% of the work of breathing, although it also has non-ventilatory
87 functions, e.g., coughing, hiccups, sneezing, vomiting, and postural functions. It is composed
88 of three main parts, see Figure 1a. There are two muscular parts, one median and horizontal
89 in upright position, separating the thoracic and the abdominal organs, and another lateral
90 muscle part, which ends with the costal insertions (attachment to the lower ribs), and there
91 is one central tendon, where the extremities of all the muscle fibers converge. When the
92 diaphragm contracts during inspiration (inhalation) with a piston-like motion, the muscle
93 zone thickens (inspiratory thickening), and the domes move caudally (downward) expanding
94 the thorax. Therefore, the air enters the lungs under a pressure gradient, see Figure 1b.

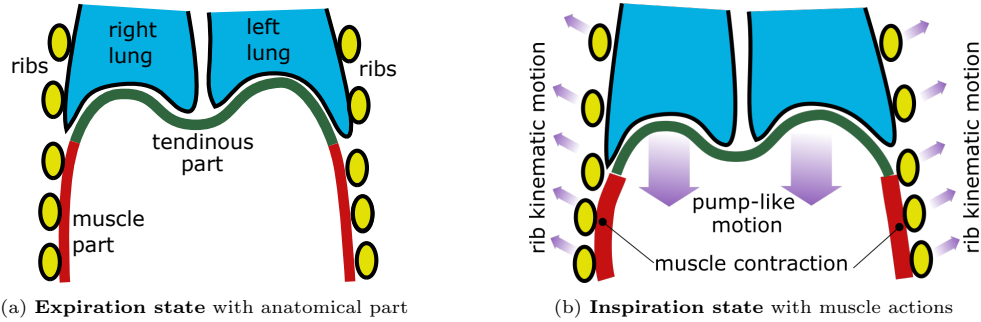


Figure 1: Anatomy and physiology of the diaphragm (red and green parts) from expiration to inspiration

95 The two-dimensional geometry used for our simulations was extracted from a real patient
 96 medical image. We used a 3D CT scan image (resolution: $0.927 \times 0.927 \times 0.3 \text{ mm}^3$) that
 97 was acquired for medical reasons, see our previous work [5]. The diaphragm was manually
 98 segmented in 3D following visual cues as explained in [17]. The labeled voxels were exported
 99 to a triangle mesh with the Marching Cube algorithm and the mesh was simplified with a
 100 decimation algorithm [18].

101 The frontal plane slice we selected is in the middle of the body, corresponding roughly
 102 to the anatomic illustration of Figure 1. The raw data consists of a list of 2D vertices
 103 where a topology can easily be extracted. The raw geometry data contains noise from
 104 several sources. There is some CT scan device incertitude (noise, calibration etc) [19], the
 105 data is the result from a discretized process, and the labeling data comes from a manual
 106 segmentation that is prone to human error. Concerning this last point, the diaphragm is not
 107 entirely visible, sometimes part of its voxels also include other organs. The accuracy is linked
 108 to the imagination and the anatomical knowledge of the medical expert that performed the
 109 segmentation.

110 The expected displacement of the diaphragm between the relaxed and contracted states
 111 in the two-dimensional slice is roughly illustrated in Figure 2. For the numerical sim-
 112 ulations in Sections 7 and 8, we construct boundary conditions to replicate this motion
 113 qualitatively.

114 3. Equations of linear elasticity

The simplified model that we use is valid for studying small deformations of an isotropic and homogenous diaphragm with a linear elasticity constitutive law. The deformation of a diaphragm Ω is described by applying a displacement field $u = (u_1, u_2)^T$, to an object location $y = (y_1, y_2)^T \in \Omega$ such that:

$$y^* = y + u,$$

where $y^* = (y_1^*, y_2^*)^T \in \Omega^*$ is then a deformed object. A field derived from the displacements is the stress tensor:

$$\sigma = \begin{pmatrix} \sigma_{11} & \sigma_{12} \\ \sigma_{21} & \sigma_{22} \end{pmatrix},$$

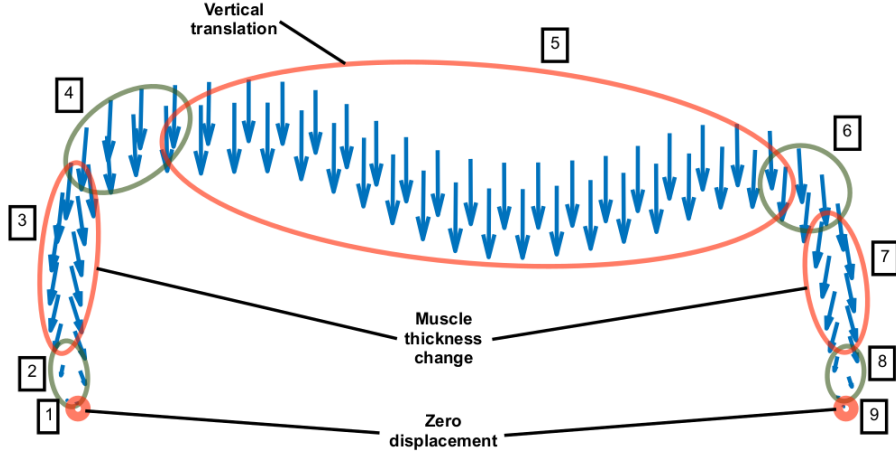


Figure 2: The expected displacement in different parts of the slice of the diaphragm. The red areas correspond to the real physiological behavior and the green areas are transition zones. In regions 3 and 7, there is both a thickening of the muscle and a downward motion, while in region 5, the downward motion dominates.

which measures the internal forces in Ω as a consequence of deformation. It is related to the displacement field by:

$$\sigma = \lambda \text{Tr}(\varepsilon) + 2\mu\varepsilon, \quad \varepsilon = \frac{1}{2} \left((\nabla u)^T + \nabla u \right), \quad (1)$$

where $\varepsilon \in \mathbb{R}^{2 \times 2}$ is the strain tensor and $\text{Tr}(\varepsilon) = (\varepsilon_{11} + \varepsilon_{22})I$ is its trace. The scalars λ and μ are the Lamé parameters, which are related to the Young modulus E and the Poisson ratio ν of the material through:

$$\lambda = \frac{E\nu}{(1+\nu)(1-2\nu)}, \quad \mu = \frac{E}{2(1+\nu)}. \quad (2)$$

For our computations we use $E = 10^5$ Pa and $\nu = 0.3$. A special stress measure that is also of interest to us is the Von Mises stress:

$$\sqrt{\sigma_{11}^2 - \sigma_{11}\sigma_{22} + \sigma_{22}^2 + 3\sigma_{12}^2}, \quad (3)$$

115 which provides a scalar measure of the total stress.

The equations of linear elasticity are derived from the force equilibrium (Newton's second law) imposed on Ω . We have:

$$-\nabla \cdot \sigma = f \text{ on } \Omega, \quad (4)$$

where $f = (f_1(y), f_2(y))^T$ is a field of internal forces in the horizontal and the vertical direction. The Dirichlet and traction boundary conditions are prescribed on two disjoint parts of the boundary, which together form the whole boundary $\partial\Omega = \partial\Omega_0 \cup \partial\Omega_1$:

$$\begin{aligned} u &= g \text{ on } \partial\Omega_0, \\ \sigma \cdot n &= h \text{ on } \partial\Omega_1. \end{aligned} \quad (5)$$

The first boundary condition with the right hand side $g = (g_1(y), g_2(y))^T$ is the displacement condition. The second boundary condition with the right hand side $h = (h_1(y), h_2(y))^T$ is the traction condition. An equivalent form of (5) is the Robin boundary condition:

$$u \kappa_0(y) + (\sigma \cdot n) \kappa_1(y) = g \kappa_0(y) + h \kappa_1(y) \text{ on } \partial\Omega = \partial\Omega_0 \cup \partial\Omega_1, \quad (6)$$

116 where κ_0 and κ_1 correspond to two spatially dependent coefficients, in this case discontin-
117 uous: $\kappa_0(y) = 1$ when $y \in \partial\Omega_0$ and zero otherwise, and $\kappa_1(y) = 1$ when $y \in \partial\Omega_1$ and zero
118 otherwise.

119 In Section 7 we first compute solutions using a Dirichlet condition for the whole boundary.
120 ($\kappa_0(y) = 1, \kappa_1(y) = 0, y \in \partial\Omega$). Then, in Section 8, we compute solutions using smoothed
121 Dirichlet and traction conditions (smooth Robin coefficients), which approximates the im-
122 position of these two conditions on two disjoint parts of the diaphragm. However, since
123 physiology suggests a smooth solution, we see this as modeling rather than as an error.

For all of the computations in this paper we use the displacement formulation of (4), obtained by using the relation between stress and displacement given in (1). The force equilibrium (4) then expands to:

$$-\nabla \cdot \sigma = -\mu \nabla^2 u - (\lambda + \mu) \nabla(\nabla \cdot u) = f,$$

and the traction boundary condition from (5) to:

$$\sigma \cdot n = \left[\lambda (\nabla \cdot u) I + \mu \left((\nabla u)^T + \nabla u \right) \right] \cdot n = h.$$

The displacement formulation of the linear elasticity equations with the boundary condition from (6) is then written as:

$$\begin{aligned} -\mu \nabla^2 u - (\lambda + \mu) \nabla(\nabla \cdot u) &= f && \text{on } \Omega, \\ u \kappa_0 + \left(\left[\lambda (\nabla \cdot u) I + \mu \left((\nabla u)^T + \nabla u \right) \right] \cdot n \right) \kappa_1 &= g \kappa_0 + h \kappa_1 && \text{on } \partial\Omega. \end{aligned} \quad (7)$$

For simplicity we rewrite the system above as:

$$Du(y) = F(y),$$

where:

$$\begin{aligned} Du(y) &= \begin{cases} D_2 u(y), & y \in \Omega \\ \kappa_0(y) D_0 u(y) + \kappa_1(y) D_1 u(y) \cdot n(y), & y \in \partial\Omega \end{cases} \\ F(y) &= \begin{cases} f(y), & y \in \Omega \\ \kappa_0(y) g(y) + \kappa_1(y) h(y), & y \in \partial\Omega \end{cases} \end{aligned} \quad (8)$$

Here D_2, D_1, D_0 are the expanded operators that in (8) correspond to $\Omega, \partial\Omega_1$ and $\partial\Omega_0$ respectively. If we let $\nabla_{ij} = \frac{\partial^2}{\partial y_i \partial y_j}$ and $\nabla_i = \frac{\partial}{\partial y_i}$, then the operator D_2 is:

$$D_2 = - \begin{pmatrix} (\lambda + 2\mu) \nabla_{11} + \mu \nabla_{22} & (\lambda + \mu) \nabla_{12} \\ (\lambda + \mu) \nabla_{12} & \mu \nabla_{11} + (\lambda + 2\mu) \nabla_{22} \end{pmatrix}, \quad (9)$$

and the boundary operators D_1 and D_0 are:

$$D_1 = \begin{pmatrix} \mu n_2 \nabla_2 + (\lambda + 2\mu) n_1 \nabla_1 & \lambda n_1 \nabla_2 + \mu n_2 \nabla_1 \\ \mu n_1 \nabla_2 + \lambda n_2 \nabla_1 & (\lambda + 2\mu) n_2 \nabla_2 + \mu n_1 \nabla_1 \end{pmatrix}, \quad D_0 = \begin{pmatrix} I & 0 \\ 0 & I \end{pmatrix}. \quad (10)$$

124 **4. Approximation of functions using the RBF-FD method**

125 Here we describe the approximation framework which is used when representing the
 126 unknown displacement and the stress (which are the outputs of the simulation), and the
 127 known data vectors (the input data to the simulation) as continuous functions. The following
 128 discussion is general in the sense that the data vector can be known or unknown. Concrete
 129 examples of using the framework developed in this section are given in later sections.

Given a data vector $\tilde{u}(X) = [\tilde{u}(x_1), \tilde{u}(x_2), \dots, \tilde{u}(x_N)]^T$ where $x_i \in \mathbb{R}^d$ we construct a semi-discrete evaluation operator $E = E(y, X)$, which, for any point $y \in \Omega \subset \mathbb{R}^d$, returns the value of the interpolant of the data $\tilde{u}(X)$ at that point, such that:

$$\tilde{u}(Y) = E(y, X)\tilde{u}(X). \quad (11)$$

Now we use (11) for each $y \in Y$ to obtain a system of equations and form the matrix $E(Y, X)$ of size $M \times N$, $M \geq N$. Note that in our notation this is equivalent to setting $y = Y$. The RBF-FD procedure constructs the matrix $E(Y, X)$ using a sequence of local, stencil-based interpolation problems which are exact for a cubic or quintic polyharmonic spline basis (PHS) and a (multivariate) monomial basis of degree p . The matrix $E(Y, X)$ is sparse, that is, it contains $n \ll N$ non-zero elements per row, where n is the stencil size defined by:

$$n = 2 \binom{p+d}{d}. \quad (12)$$

Details about using PHS plus the monomial basis in RBF-FD approximations can be found in [20, 21, 22, 23]. In the same way, we construct a semi-discrete operator for differentiation $D^{\mathcal{L}} = D^{\mathcal{L}}(y, X)$ which locally evaluates any derivative \mathcal{L} of $\tilde{u}(Y)$:

$$\mathcal{L}\tilde{u}(Y) = D^{\mathcal{L}}(y, X)\tilde{u}(X). \quad (13)$$

130 Both matrices, $E(Y, X)$ and $D^{\mathcal{L}}(Y, X)$, can be formed using the MATLAB code avail-
 131 able in [24]. For completeness, we below provide the steps to compute the matrix elements
 132 (weights) and to assemble $D^{\mathcal{L}}(Y, X)$ and $E(Y, X)$ for the point sets Y and X in any dimen-
 133 sion d .

- 134 1. Let $x_1^{(k)} = x_i \in X$ (one stencil center) and find n closest neighbors $\{x_j^{(k)}\}_{j=1}^n$ (stencil
 135 points) around it using the Euclidean distance.
- 136 2. Scale and shift the stencil points to a unit domain $[-1, 1]^d$. Save the scaling as $s^{(k)}$.
- 137 3. Form a square interpolation matrix $A^{(k)}$, where $A_{ij}^{(k)} = r^3 = \|x_i^{(k)} - x_j^{(k)}\|_2^3$ and
 138 $x_i^{(k)}, x_j^{(k)}$, $i, j = 1, \dots, n$ belong to the stencil.
- 139 4. Form a rectangular polynomial matrix $P^{(k)}$, where $P_{il}^{(k)} = p_l(x_i^{(k)})$, $i = 1, \dots, n$, $l =$
 140 $1, \dots, m$ is a sampled d -dimensional monomial basis with m basis functions. When n is
 141 chosen as in (12) then $m = \frac{n}{2}$ and the size of the matrix $P^{(k)}$ is $n \times \frac{n}{2}$.
- 142 5. Using $A^{(k)}$ and $P^{(k)}$, form the augmented local interpolation matrix:

$$\tilde{A}^{(k)} = \begin{pmatrix} A^{(k)} & P^{(k)} \\ (P^{(k)})^T & 0 \end{pmatrix} \quad (14)$$

- 142 6. Repeat steps 1–5 for every $x \in X$ in order to form all $\tilde{A}^{(k)}$.

143 The local evaluation and differentiation weights can then be computed in the following way:

- 144 1. Take one evaluation point $y_l \in Y$ and find the first closest point from the X point set.
145 We denote it by $x_1^{(k)}$.
- 146 2. Scale y_l to a unit domain $[-1, 1]^d$ using the previously computed scaling $s^{(k)}$.
- 147 3. Form a vector $b_1 = \mathcal{L} \|y_l - x_j^{(k)}\|_2^3$, where $\{x_j^{(k)}\}_{j=1}^n$ is the local neighborhood of the
148 center point $x_1^{(k)}$, where $\mathcal{L} = 1$ for constructing evaluation weights, or a derivative
149 operator for constructing differentiation weights.
- 150 4. Form a vector $b_2 = \mathcal{L} p_j(y_l)$, $j = 1, \dots, \frac{n}{2}$.
- 151 5. Concatenate the two vectors into $b(y_l) = [b_1, b_2]$.
- 152 6. Use the augmented interpolation matrix that belongs to $x_1^{(k)}$ and compute the local
153 weights by using the relation $w_{\mathcal{L}}(y_l) = (\tilde{A}^{(k)})^{-1} b_{\mathcal{L}}(y_l)$.
- 154 7. Store $w_{\mathcal{L}}(y_l)$ in the l -th row of the matrix $W_{\mathcal{L}}(Y)$.
- 155 8. Repeat steps 1–6 for every $y_l \in Y$ in order to form all local weights.

156 When using these steps to compute the weights, it is possible to avoid storing the matrix $\tilde{A}^{(k)}$
157 by combining the two parts such that the evaluation/differentiation weights are computed
158 for all y_l which select $x_1^{(k)}$ as its closest stencil center, immediately after step 5 of the first
159 list. Once the matrix of local weights $W_{\mathcal{L}}(Y)$ of size $M \times n$ is computed, these weights
160 are assembled into a global rectangular matrix, $E(Y, X)$ for evaluation and $D_{\mathcal{L}}(Y, X)$ for
161 differentiation, both of size $M \times N$. This can be done by using a matrix $\Gamma \in \mathbb{Z}^{N \times n}$, which
162 is a list of indices of the local neighborhoods of points around every stencil point $x_1^{(k)} \in X$.
163 Additionally, a matrix $\kappa \in \mathbb{Z}^{M \times 1}$ is needed, which is a list of indices of the stencil centers
164 that are closest to each evaluation point y_l . Γ and κ are found using the k-nearest neighbor
165 method with k equal to n and 1, respectively. Using the MATLAB programming language,
166 the two lists and the sparse matrix can be efficiently computed by invoking the following
167 three commands:

```
168     Gamma = knnsearch(X,X, 'k', n)
169     kappa = knnsearch(X,Y, 'k', 1)
170     D_L = sparse(repmat(1:M, 1, n), Gamma(kappa,:), W_L, M, N, N*n)
```

171 where the first two arguments to the function `sparse()` have the same shape as $W_{\mathcal{L}}(Y)$
172 and contain the row and column indices for inserting the locally computed weights into the
173 global matrix.

174 5. Discretization of the linear elastic model using the unfitted RBF-FD method

175 In this section we employ the unfitted RBF-FD method [7] to discretize the linear elas-
176 ticity equations (8), (9) and (10) over the diaphragm. The method relies on constructing
177 rectangular differentiation matrices $D^{\mathcal{L}}(Y, X)$ as described in Section 4. The matrices then
178 replace the differential operators in the PDE, together with the corresponding discrete right
179 hand sides $F(Y)$.

180 To form the differentiation matrices, we first decide the degree p of the monomial basis
181 that we are appending to the PHS approximation, and compute the stencil size n using
182 (12). Then we construct an interpolation point set X that extends over the diaphragm (see
183 Figure 3), and an evaluation point set Y (see Figure 4) that conforms to the geometry of
184 the diaphragm. Those two point sets are obtained in four simple steps:

- 185 • The initial point set X_1 is a tilted Cartesian node layout with spacing h in a box that
186 encloses the diaphragm. (the grey and blue points in Figure 3).

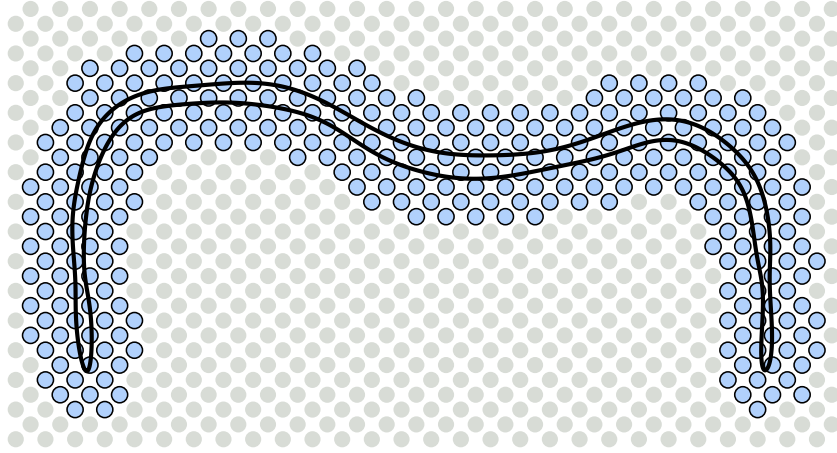


Figure 3: The initial point set X_1 (tilted Cartesian points) is distributed over a box that encloses the boundary of the diaphragm (black curve). Points that are more than half a stencil size away from the geometry (grey) are removed. The remaining points (blue) form the point set X .

- 187 • Then the point set Y_1 is generated by placing q points with average spacing h_y in each
188 Voronoi region inside the diaphragm, defined by the points in X_1 . (the red points in
189 Figure 4).
- 190 • In addition, the point set Y_b with the same average spacing h_y is generated by placing
191 points along the boundary of the diaphragm, see Figure 4.
- 192 • The final evaluation point set is given by $Y = Y_1 \cup Y_b$, see Figure 4.
- 193 • The final node set X (the blue points in Figure 3 and Figure 4) is formed by reducing
194 X_1 by removing points that fall more than half stencil size outside the diaphragm. In
195 Matlab this can be done by:

```
196 X = X_1(unique(knnsearch(X_1,Y,'k',ceil(0.5*n)), :), :);
```

197 The last step ensures that the columns of $E(Y, X)$ and $D^{\mathcal{L}(Y, X)}$ are non-zero [7]. Note
198 that the evaluation point set does not need to be constructed by placing precisely q points
199 in every Voronoi region. It is possible to use any global point set, which is quasi-uniform
200 by nature (e.g. Halton points), and as such on average samples every Voronoi region with
201 approximately q points.

202 Next, we use the method described in Section 4 to discretize the continuous operator
203 D_2 in (9) using the interior evaluation points Y_1 , and to discretize the continuous operators
204 D_1 and D_0 in (10) using the boundary evaluation points Y_b . We let $D_k^{ij}(\cdot, X)$ denote the
205 differentiation matrix that approximates element i, j , of the operator D_k , $k = 0, 1, 2$. If we

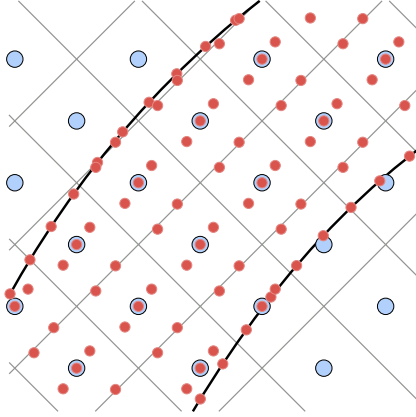


Figure 4: The black curve represents a part of the boundary of the diaphragm. Node points in X (blue markers) and the corresponding Voronoi regions (grey lines) are shown together with interior evaluation points, Y_1 , and boundary evaluation points, Y_b , (red markers). The same template of interior evaluation points is used in each Voronoi region inside the diaphragm geometry.

206 let $i, j = 1, 2$, while $i \neq j$, then we can express the differentiation matrices as:

$$\begin{aligned}
D_2^{ii}(Y_1, X) &= (\lambda + 2\mu)D^{\nabla ii}(Y_1, X) + \mu D^{\nabla jj}(Y_1, X), \\
D_2^{ij}(Y_1, X) &= (\lambda + \mu)D^{\nabla ij}(Y_1, X), \\
D_0^{ii}(Y_b, X) &= E(Y_b, X), \\
D_0^{ij}(Y_b, X) &= 0, \\
D_1^{ii}(Y_b, X) &= (\lambda + 2\mu)n_i D^{\nabla i}(Y_b, X) + \mu n_j D^{\nabla j}(Y_b, X), \\
D_1^{ij}(Y_b, X) &= \lambda n_i D^{\nabla j}(Y_b, X) + \mu n_j D^{\nabla i}(Y_b, X).
\end{aligned}$$

We express the discrete Robin coefficients as $K_i(Y_b) = \text{diag}(\kappa_i(Y_b))$, $i = 0, 1$, and introduce a scaling β_i for equations connected with the operator D_i . Finally, we form the rectangular system of size $2M \times 2N$ that discretizes the Navier-Cauchy system with Robin boundary conditions (8):

$$\begin{pmatrix}
\beta_2 D_2^{11} & \beta_2 D_2^{12} \\
\beta_2 D_2^{21} & \beta_2 D_2^{22} \\
\beta_0 K_0 D_0^{11} + \beta_1 K_1 D_1^{11} & \beta_1 K_1 D_1^{12} \\
\beta_1 K_1 D_1^{21} & \beta_0 K_0 D_0^{22} + \beta_1 K_1 D_1^{22}
\end{pmatrix}
\begin{pmatrix}
\tilde{u}_1(X) \\
\tilde{u}_2(X)
\end{pmatrix}
=
\begin{pmatrix}
\beta_2 f_1(Y_1) \\
\beta_2 f_2(Y_1) \\
\beta_0 K_0 g_1(Y_b) + \beta_1 K_1 h_1(Y_b) \\
\beta_0 K_0 g_2(Y_b) + \beta_1 K_1 h_2(Y_b)
\end{pmatrix}. \quad (15)$$

In the numerical experiments, we use the following scale factors:

$$\beta_2 = \frac{1}{\mu} h_y, \quad \beta_1 = \frac{10}{\mu} \frac{1}{h} h_y^{\frac{1}{2}}, \quad \beta_0 = \frac{1}{h} h_y^{\frac{1}{2}}, \quad (16)$$

where h and h_y are the average internodal distances in the X and Y point sets, respectively. These are computed as:

$$h = \frac{1}{N} \sum_{j=1}^N \min_{i \neq j} \|x_i - x_j\|_2, \quad h_y = \frac{1}{M} \sum_{j=1}^M \min_{i \neq j} \|y_i - y_j\|_2. \quad (17)$$

207 The choice of scale factors is based on the papers [7, 8], where the scale factors h_y for
 208 the interior and $h_y^{1/2}$ for the boundary are used, such that the norms of the discrete least
 209 squares problem approximate the continuous L_2 -norm. The additional $1/h$ scaling increases
 210 the weight of the boundary conditions and improves convergence. The Lamé parameter μ
 211 is large and affects the scaling between different equations. Therefore, we also include the
 212 factor $10/\mu$ in β_1 .

We solve the least-squares problem (15), for the nodal values $\tilde{u}_1(X)$ and $\tilde{u}_2(X)$, using
 backslash in MATLAB. After that the solution is evaluated at the Y point set, using the
 evaluation matrix E :

$$\tilde{u}_1(Y) = E(Y, X) \tilde{u}_1(X), \quad \tilde{u}_2(Y) = E(Y, X) \tilde{u}_2(X). \quad (18)$$

213 The strains and the stresses (1), (3) are computed by applying appropriate differentiation
 214 matrices to the solution coefficients $\tilde{u}_1(X)$ and $\tilde{u}_2(X)$.

215 6. Smoothing of geometry and boundary data

If we view the two-dimensional diaphragm from the continuous perspective, the geometry
 can be described as a closed curve. We choose to parametrize this curve by $t \in [0, 2\pi]$,
 where the starting point $t = 0$ is the same as the final point $t = 2\pi$. To benefit from the
 potential high-order convergence of the unfitted RBF-FD method, we need to approximate
 the boundary curve and the boundary data as functions of t with enough smoothness that
 the convergence of the PDE problem is not adversely affected. To avoid reduced accuracy
 due to boundary errors near the artificial end points of the interval, we extend the domain
 periodically to $t \in [-2\pi, 4\pi]$ for the approximation. We discretize the extended domain
 using the uniformly spaced node points $T = \{t_j\}_{j=1}^{N_g}$. Given \tilde{M}_g data points, we replicate
 these periodically to get the extended data set $(T^d, G) = \{(t_i^d, g_i)\}_{i=1}^{\tilde{M}_g}$, where $\tilde{M}_g = 3\tilde{M}_g >$
 N_g . We use a one-dimensional RBF-FD approximation, based on a quintic PHS basis
 augmented with polynomials of degree $p_g = 6$, to form an overdetermined linear system for
 the nodal values $g(T)$

$$E_g(T^d, T)g(T) = G. \quad (19)$$

To enforce continuity at $t = 0$, we add the following equality constraints

$$\frac{d^s g(0)}{dt^s} - \frac{d^s g(2\pi)}{dt^s} = 0, \quad s = 0, \dots, p_g - 1, \quad (20)$$

and solve the constrained least squares problem

$$\begin{pmatrix} 2E_g^T E_g & B_g^T \\ B_g & 0 \end{pmatrix} \begin{pmatrix} g(T) \\ \lambda \end{pmatrix} = \begin{pmatrix} 2E_g^T G \\ 0 \end{pmatrix}, \quad (21)$$

216 where B_g contains the p_g constraints (20) and λ contains the corresponding Lagrange mul-
 217 tipliers.

218 To find the smooth boundary curve from the initial vertex data $\tilde{x}_i^d, i = 1, \dots, \tilde{M}_g$, we first
 219 scale the data such that $x_i^d = (p_i, q_i) = s_\Omega \tilde{x}_i^d, i = 1, \dots, \tilde{M}_g$, where $s_\Omega = 156.92^{-1} \text{mm}^{-1}$.
 220 The scaling was chosen such that all data points fall within $[-1, 1]^2$. Then we compute an
 221 approximate arclength parametrization using the Euclidean distance between the scaled
 222 vertices, such that $t_i^d = 2\pi \sum_{j=1}^{i-1} \|x_{j+1}^d - x_j^d\| / \sum_{j=1}^{\tilde{M}_g} \|x_{j+1}^d - x_j^d\|$, where $x_{\tilde{M}_g+1}^d = x_1^d$.

223 Then we replicate the data over the extended domain. Finally, system (21) is solved for
 224 each coordinate function $p(t)$ and $q(t)$. The resulting boundary curve is shown in Fig-
 225 ure 5 and the individual coordinate functions are shown in Figure 6. Since the curve
 226 parametrization here is in the clockwise direction, the outward normals are computed as
 $n(t) = (-q'(t), p'(t)) / \|(-q'(t), p'(t))\|$.

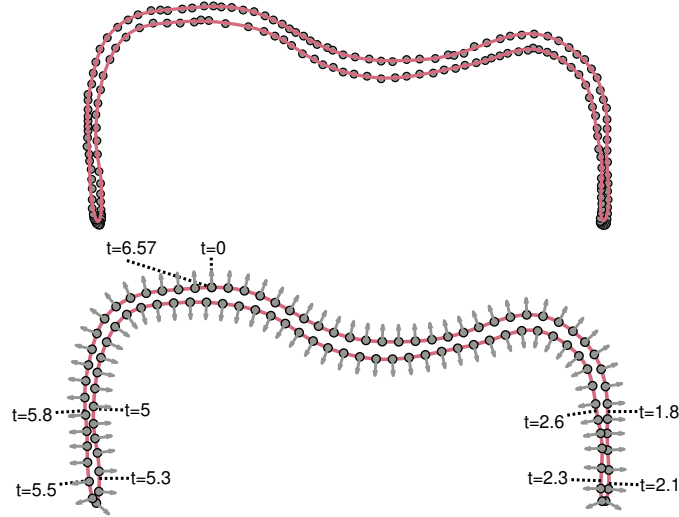


Figure 5: The smoothed boundary geometry curve (solid line) is shown in both subfigures. The curve was computed using $N_g = 133$ node points, $M_g = 177 \cdot 3 = 531$ data points, and stencil size $n = 28$. The markers show the $M_g = 177$ vertex data points (top) and uniform evaluation points (bottom). The normals computed from the approximation, as well as the values of the parameter t along the curve, are also shown in the bottom subfigure.

227

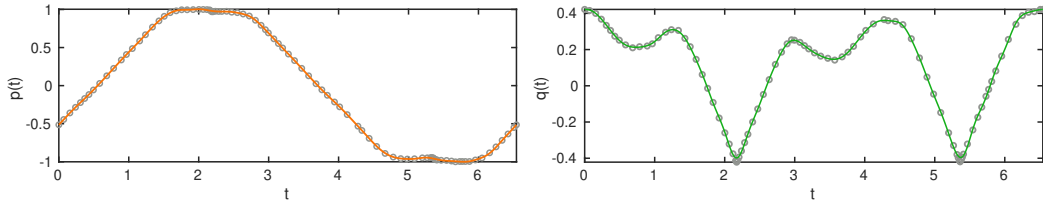


Figure 6: The two smoothed coordinate functions approximating the geometry. The function $p(t)$ (left) corresponds to the horizontal coordinate and $q(t)$ (right) corresponds to the vertical coordinate. The markers show the initial data locations.

228 For the boundary data functions g and h in (7), we manufacture data to mimic the
 229 expected physiological behaviour shown in Figure 2. A few data points are placed in the
 230 regions where we have some information (regions 1, 3, 5, 7, and 9 in Figure 2), and then the
 231 rest of the data is generated through linear interpolation. This results in gradual transitions
 232 in the regions where we lack information. The data points and the resulting curves are
 233 shown in Figures 7 and 15.

234 **7. Benchmark I: Deformation of the diaphragm using the smoothed Dirichlet**
 235 **boundary conditions**

236 In this section we solve the discretized linear elasticity equations (15). We are interested
 237 in whether the problem with smoothed Dirichlet boundary condition leads to a high-order
 238 convergence. A point of interest is also whether the resulting deformation is physiologically
 239 sensible, and whether the Von Mises stress is distributed as expected.

240 The boundary condition that we use is purely Dirichlet, which means that we set the
 241 Robin coefficients in (8) to $\kappa_0(y) = 1$ and $\kappa_1(y) = 0$. Then the only boundary data functions
 242 present in the system (15) are $g_1(y)$ and $g_2(y)$, which correspond to the imposition of
 243 displacements in the horizontal and vertical direction, respectively.

244 *7.1. The imposition of boundary displacements*

245 The displacements have been synthesized to reproduce the physiological behavior de-
 246 scribed in Section 2. Particularly, the translation of the horizontal part of the diaphragm
 247 (region 5) has been defined as a constant vertical displacement in the downward direction
 248 and the thickening of the appositional zone (regions 3 and 5) is also prescribed as a constant.
 249 As described in Section 6, we place a few data points based on this information, and then
 250 the rest of the data is generated by linear interpolation. From a physiological perspective
 251 all displacements should be smooth. We generate a smooth function by solving the con-
 252 strained least squares problem (21). The results are shown in Figure 7. Imposing smooth
 253 boundary data makes it possible to obtain high-order convergence and provides a solution
 that is physically relevant. In Figure 8 we display the boundary of the diaphragm before

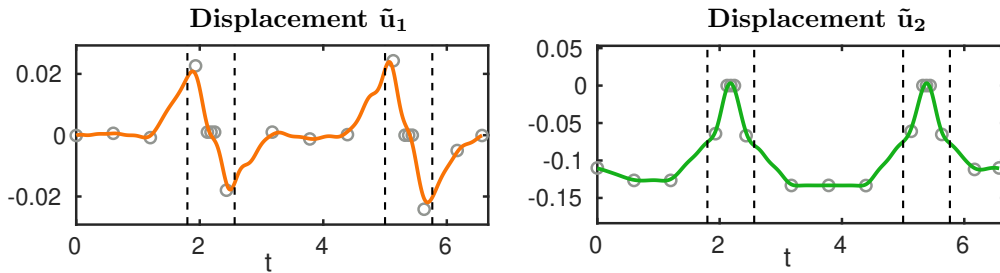


Figure 7: Benchmark I: The displacement in the horizontal direction (left) and the vertical direction (right) as a function of the boundary parametrization t (see Figure 5, right image, for an illustration of t in relation to the boundary). The markers show the initially placed data points, which are then linearly interpolated into $\tilde{M}_g = 80$ data points. For the approximation, $N_g = 120$ node points and stencil size $n = 28$ were used. The dashed lines show the location of the end points of the diaphragm (regions 2 and 8 in Figure 2).

254 and after application of the displacements from Figure 7.
 255

256 *7.2. Solution of Benchmark I*

257 The solution is given in Figure 9, where we display the spatial distribution of the dis-
 258 placements and the Von Mises stress. Looking at the \tilde{u}_1 distribution in the figure, we can
 259 observe thickening of the diaphragm in regions 2, 3, 7 and 8 according to the labels from
 260 Figure 2. Next, the distribution of \tilde{u}_2 indicates that translation is largest in regions 4, 5 and
 261 6. The Von Mises stress is largest at the interfaces between regions 2, 3 and regions 7, 8.
 262 This makes sense, since the change in the thickness is largest in these regions. We conclude
 263 that the behavior roughly follows the physiological cues described in Section 2.

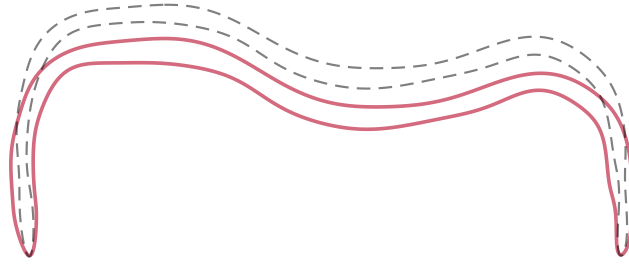


Figure 8: Benchmark I: The diaphragm in its non-deformed state (dashed line) and after displacement of the boundary (solid line).

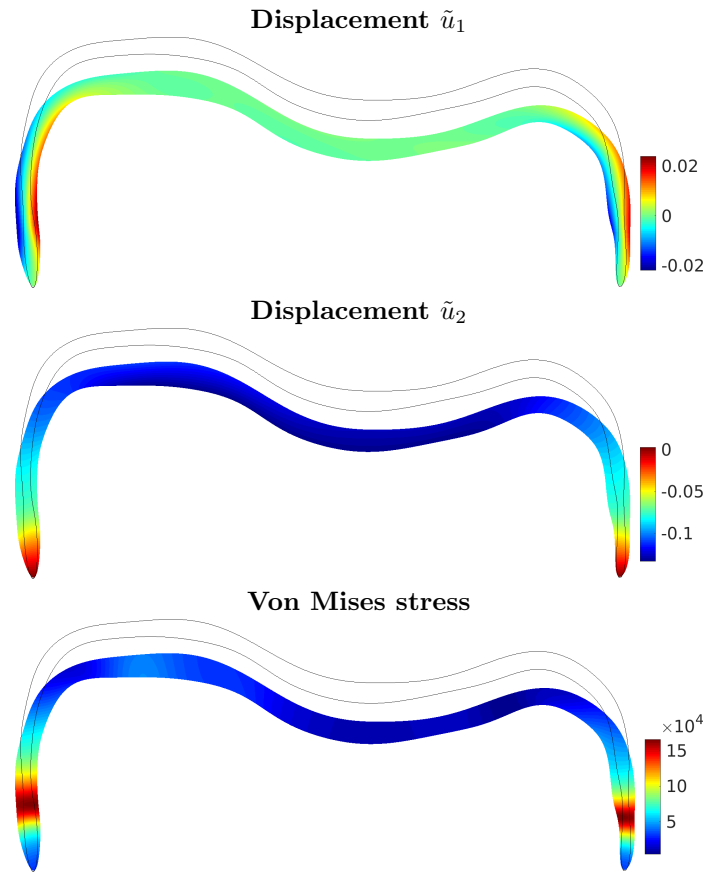


Figure 9: Benchmark I: The computed displacements and the corresponding von Mises stress over the diaphragm. This solution was obtained using the unfitted RBF-FD discretization with internodal distance $h = 0.004$, oversampling parameter $q = 5$, and an appended polynomial basis of degree $p = 5$. Due to the scaling applied to the geometry (see Section 6), the displayed results for displacement and stress should be multiplied with $s_{\Omega}^{-1} = 0.15692$ m to recover the results corresponding to the unscaled problem.

While the solution is roughly what we expect from a physiological perspective, we are yet to understand whether the simulation gives a correct answer from a numerical perspective. We investigate the convergence of the numerical solution under node refinement using several different polynomial degrees in the stencil-based approximation. Since we do not know what the true solution is, we measure convergence of the numerical solution $\tilde{u}(Y)$ towards a numerical reference solution $\tilde{u}_*(Y_*)$, where the node set is highly refined. We choose two numerical references: (i) computed using the unfitted RBF-FD-LS method with internodal distance $h = 0.002$, leading to $N = 43\,841$ and polynomial degree $p = 5$, (ii) computed using the Galerkin finite element method with linear elements and 236 414 degrees of freedom (corresponding to $h = 0.00085$), using the GetDP solver [25]. Every numerical solution \tilde{u} that we obtain is interpolated, consistent with the approximation order, to the point set of the reference solution Y_* , where we then compute the approximation error:

$$\|e\|_{\ell_2} = \frac{\|\tilde{u}(Y_*) - \tilde{u}_*(Y_*)\|_2}{\|\tilde{u}_*(Y_*)\|_2}. \quad (22)$$

Table 1 shows the relation between the internodal distance h , computed according to (17),

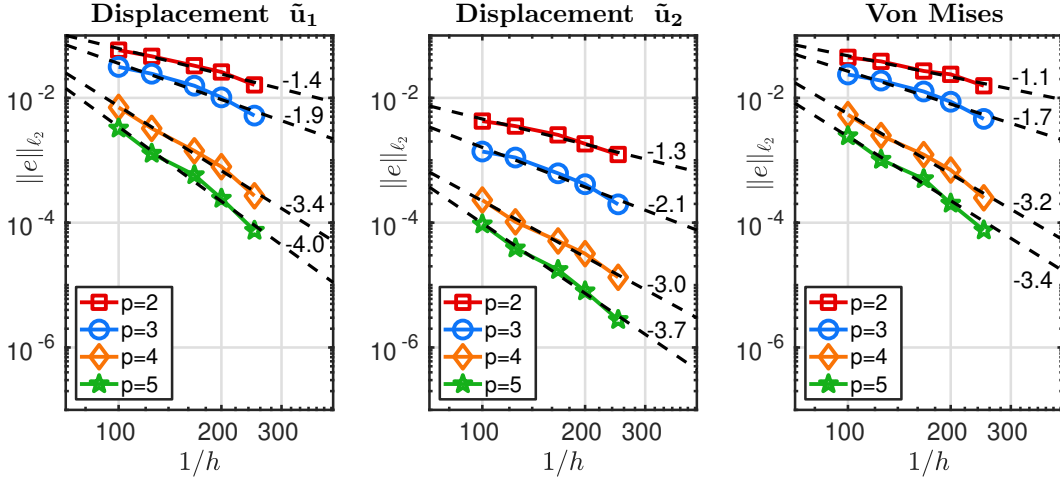


Figure 10: Benchmark I: Convergence of the displacements \tilde{u}_1 and \tilde{u}_2 and the Von Mises stress for different polynomial degrees p , against a highly resolved numerical solution computed using the unfitted RBF-FD-LS method, with $h = 0.002$ and $p = 5$.

265

and the number of degrees of freedom N for the considered problem sizes.

Table 1: Benchmark I and II: The relation between the inverse internodal distance $1/h$ and (i) the internodal distance h and (ii) the number of interpolation points N used for discretizing the PDE problem (8).

$1/h$	25	50	100	125	166.67	200	250	500
h	0.04	0.02	0.01	0.008	0.006	0.005	0.004	0.002
N	337	853	2500	3617	5904	8126	12129	43841

266

267

268

The results when the unfitted RBF-FD method is used as a reference are displayed in Figure 10. We observe that the error is small for all polynomial degrees. The convergence

269 rate increases as p is increased. For all p the convergence rates of the displacements are
 270 close to $p - 1$. The convergence rate of the Von Mises stress is larger than $p - 2$ for every p .
 271 Stress is computed using the first derivatives of the displacements, which (in theory) lowers
 272 the convergence rate with one order.

273 The results when the finite element method is used as a reference are given in Figure 11.
 274 The convergence plots for the displacement are very similar to the results in Figure 10.
 275 The convergence rate of the stress for $p = 5$ is lower compared with the self-reference test
 276 provided in Figure 10. Furthermore, when $p = 5$, the convergence seems to be stalling
 277 at the last point of observation. Our speculative reasoning is that the derivatives in the
 278 finite element space do not approximate the stresses well enough there. This implies that
 279 the FEM mesh is too coarse to match the accuracy of the unfitted RBF-FD method for
 280 derivative approximation, when the polynomial degree is as high as $p = 5$, for the range of
 h used here.

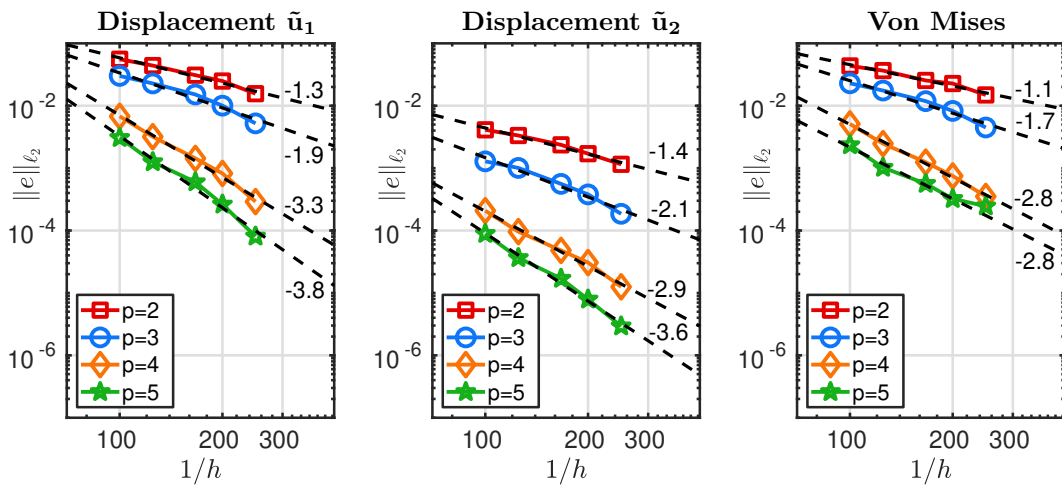


Figure 11: Benchmark I: Convergence of the displacements \tilde{u}_1 and \tilde{u}_2 and the Von Mises stress for different polynomial degrees p , against a highly resolved numerical solution computed using FEM (the GetDP solver [25]) with linear elements and 236 414 degrees of freedom (corresponding to $h = 0.00085$).

281 The spatial distribution of the error when using the self-reference solution and the finite
 282 element reference solution is shown in Figure 12 and Figure 13, respectively. The numerical
 283 solution was computed using $h = 0.004$, $q = 5$, $p = 5$. For all solution fields and both
 284 references we can observe that the error is larger in the regions with larger Von Mises stress.
 285 In addition, the error also tends to be larger in the regions where the boundary curve is
 286 concave. This implies that our problem could benefit from adaptive node refinement, which
 287 we are planning to use in our future work.
 288

289 8. Benchmark II: Deformation of the diaphragm using the smoothed Robin 290 boundary conditions

291 This benchmark includes a more difficult problem compared with Benchmark I from Sec-
 292 tion 7. As discussed in Section 2, we can measure the displacements over certain parts of the
 293 boundary, i.e., where the diaphragm is fixed near the spine, or where it moves together with

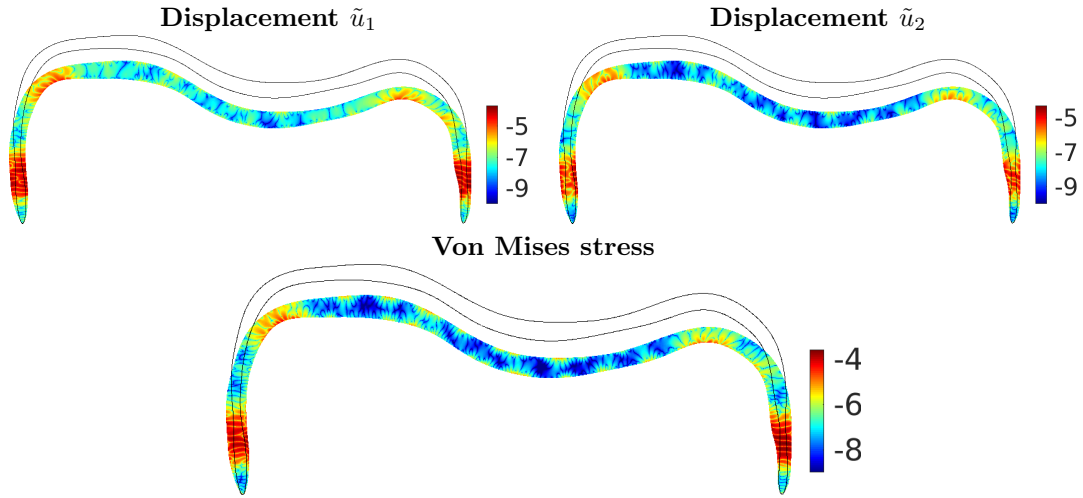


Figure 12: Benchmark I: Error distribution in logarithmic scale for $h = 0.006$ and $p = 5$ when a fine unfitted RBF-FD-LS solution ($h = 0.002$, $p = 5$) is taken as reference for computing the error.

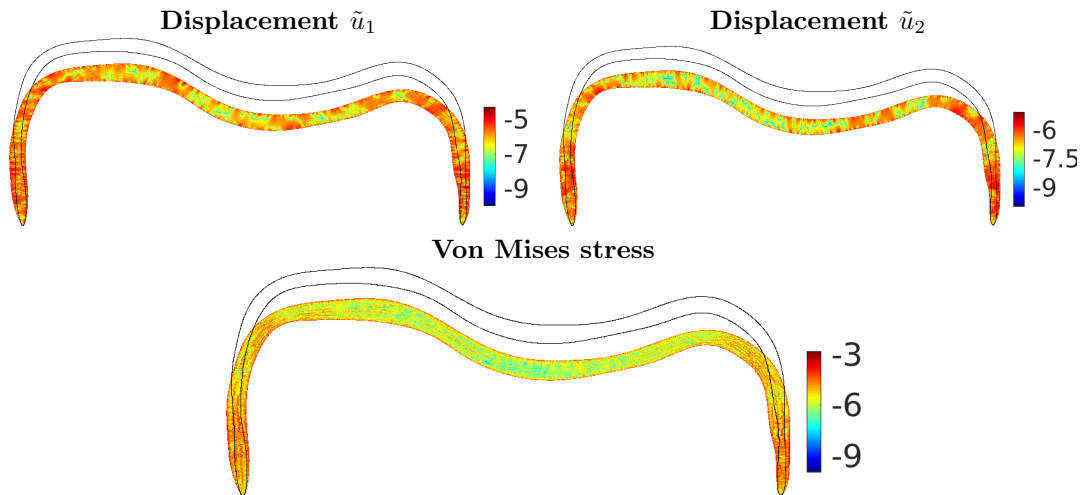


Figure 13: Benchmark I: Error distribution in logarithmic scale for $h = 0.006$ and $p = 5$ when a fine unfitted RBF-FD-LS solution ($h = 0.002$, $p = 5$) is taken as reference for computing the error.

294 the sternum and some ribs. In the regions where the displacements are not known, we may
 295 instead have information about the thoracic or abdominal pressure. A pressure condition
 296 is a special case of a traction boundary condition. A straightforward way to handle these
 297 boundary conditions would be to impose the Dirichlet condition (the known displacements)
 298 and the traction condition (the known traction values) in disjoint regions. This implies a
 299 discontinuous imposition of boundary conditions, for which: (i) we can not obtain high-
 300 order convergence according to our preliminary tests, (ii) the resulting deformation might
 301 be discontinuous or have large local derivatives, which would not reflect the physiological
 302 behavior of the diaphragm. For this reason we introduce a smooth blending of the Dirichlet

303 and the traction boundary conditions in Robin form (6).

304 This setting implies that we solve the system of equations (15), where the supports of
 305 the Robin coefficients $\kappa_0(y)$ and $\kappa_1(y)$ are chosen to overlap slightly in the regions where
 306 the type of boundary data changes. In Figure 14 we display the Robin coefficients which we
 307 use in Benchmark II. The displayed coefficients are a function of the boundary parameter
 308 t . The coefficients were computed using a sum of the sigmoid functions $\frac{1}{1+e^{\varepsilon(t-d_i)}}$, where
 309 $\varepsilon = \pm 20$, t is the boundary parameter and d_i , $i = 1, 2, \dots$ are the transition points (marked
 310 by dashed lines in Figure 14). The sign of ε depends on whether the coefficient is increasing
 311 (positive sign) or decreasing (negative sign).

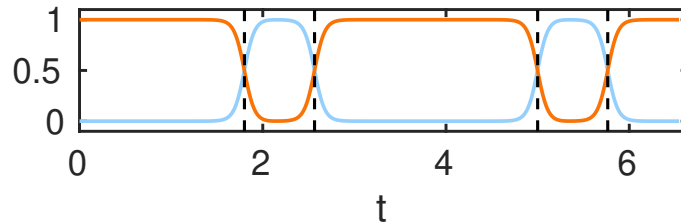


Figure 14: The Robin boundary coefficients displayed over the diaphragm show the impositions of the traction and the Dirichlet parts of the boundary condition. The orange line corresponds to the traction coefficient κ_1 , and the blue line corresponds to the Dirichlet coefficient κ_0 . The dashed lines show the location of the end points of the diaphragm (regions 2 and 8 in Figure 2). The parameter t corresponding to the boundary of the diaphragm is illustrated in Figure 5.

312 The smoothed boundary displacement values g_1 , g_2 and the boundary traction values
 313 h_1 , h_2 are given in Figure 15. Through the functions g_1 and g_2 we impose thickening in the
 314 regions 2, 3, 7 and 8 based on the distribution in Figure 2. Additionally, we also impose
 315 a gentle translation in the negative vertical direction in the regions 7 and 8. Through the
 316 functions h_1 and h_2 we impose the translation of zone 5 in the negative vertical direction.

317 8.1. Solution of Benchmark II

318 The solution is given in Figure 16, where we can see the spatial distribution of displace-
 319 ments and the Von Mises stress. To obtain this figure we used $h = 0.006$, $p = 5$, and
 320 $q = 5$. We observe that there is a slight thickening in regions 2, 3, 7 and 8, according to the
 321 labels from Figure 2, which corresponds to the imposed thickening up to some extent. In
 322 regions 4 and 6, we observe a slight bend towards the interior, and in region 5, a translation
 323 in the negative vertical direction. This behavior does not entirely mimic the physiological
 324 contraction of the diaphragm, however, constructing a more accurate model is planned as
 325 future work. This solution serves as a test to understand whether the unfitted RBF-FD
 326 method can handle the problem with the smoothed Robin boundary condition, as well as
 327 to explore how this type of boundary condition affects the behaviour of the solution.

328 8.2. Convergence under node refinement

329 We validate the numerical solution by studying convergence under node refinement. Our
 330 choice of reference solution for this study is a fine solution computed using the unfitted RBF-
 331 FD method with an internodal distance $h = 0.002$ and a polynomial degree $p = 5$ used for
 332 constructing the local approximations. The relative error against the reference solution is
 333 computed using (22). The relation between the considered h and the number of points N
 334 in X is given in Table 1.

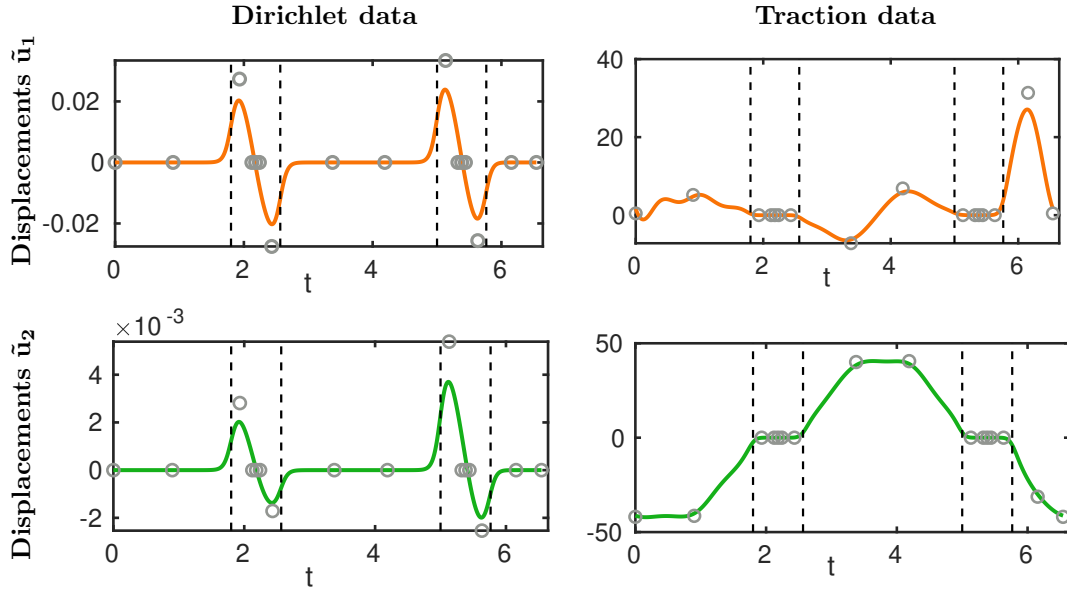


Figure 15: Benchmark II: The smoothed boundary data over the diaphragm. For this benchmark we have both Dirichlet data (left column) and traction data (right column), each with a horizontal component (first row) and a vertical component (second row). The markers show the initially placed data points, which are then linearly interpolated into $M_g = 80$ data points. For the approximation, $N_g = 120$ node points and stencil size $n = 28$ were used. The dashed lines show the location of the end points of the diaphragm (regions 2 and 8 in Figure 2). The parameter t corresponding to the boundary of the diaphragm is illustrated in Figure 5 (right image).

335 The errors for different choices of the polynomial degree p are displayed in Figure 17.
 336 We do not observe convergence for any p when h is too large. The reason for this is that
 337 the problem is not resolved yet. When h is sufficiently small, and when $p = 4$ or $p = 5$,
 338 the solution converges at least with order $p - 1$, which is desired. When $p = 2$, we do not
 339 see convergence, since we would need an even higher resolution for this (small) polynomial
 340 degree. When $p = 3$ we observe an approximately first order convergence for a sufficiently
 341 small h . This order is expected to increase to $p - 1 = 2$ if h is refined further. Low-order or
 342 no convergence when p is small advocates using a higher order method.

343 The spatial distribution of the error computed using $h = 0.006$ and $p = 5$ is given in
 344 Figure 18. Here the error is largest close to region 5 from Figure 2, where we have enforced
 345 the traction boundary condition, which includes derivatives. In our experience the error is
 346 normally larger in the regions where derivative boundary conditions are imposed compared
 347 with the regions where a Dirichlet condition is imposed, and we also observed this in [7, 8].
 348

349 9. Conclusions

350 The unfitted RBF-FD method in the least-squares setting [7] provided a robust frame-
 351 work for solving the linear elasticity system of PDEs over the simplified diaphragm geometry.

352 We could also use the unfitted RBF-FD method to smooth the geometry curve and the
 353 boundary data. Ensuring that all components of the model were smooth allowed us to

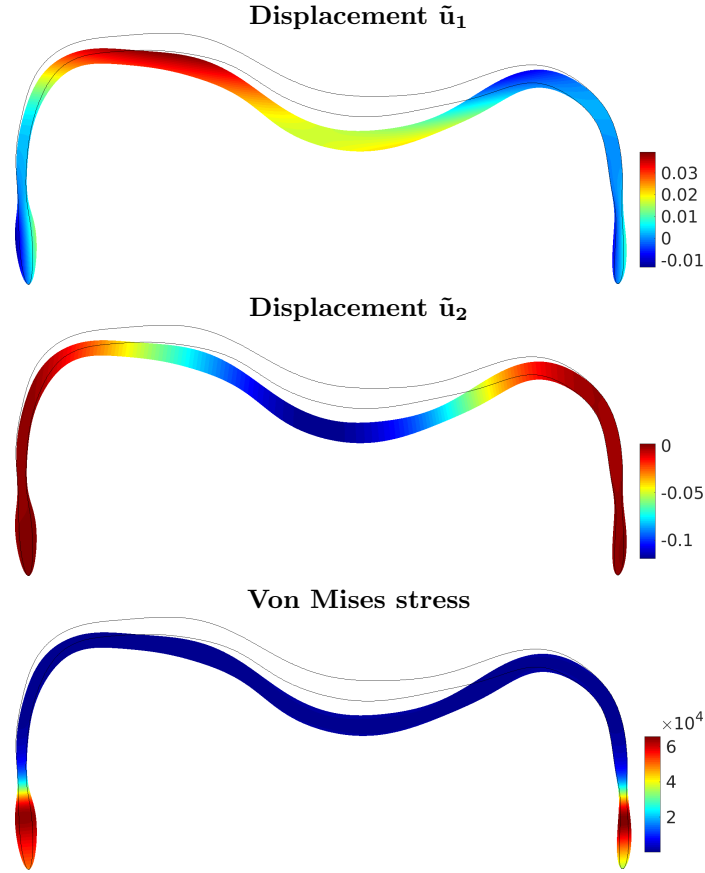


Figure 16: Benchmark II: The computed displacements and the corresponding von Mises stress over the diaphragm. This solution was obtained using the unfitted RBF-FD discretization with internodal distance 0.006, an oversampling parameter $q = 5$ and an appended polynomial basis of degree $p = 5$. Due to the scaling applied to the geometry (see Section 6), the displayed results for displacement and stress should be multiplied with $s_{\Omega}^{-1} = 0.15692$ m to recover the results corresponding to the unscaled problem.

354 achieve high-order convergence, which reduces the number of unknowns needed for a given
 355 approximation error. In the experiments (not unexpectedly), Benchmark II, with Robin
 356 boundary conditions, proved more challenging to solve than Benchmark I with Dirichlet
 357 conditions. We needed higher resolution to achieve the same error level, and we did not
 358 see any convergence for the larger values of h . In the error plots, we could also see that
 359 the error is largest in the area where only the traction condition is active. In the present
 360 work, we manufactured the data for the boundary conditions, but the aim is to eventually
 361 use measured pressure values and the solid body rotation of the ribs as boundary input
 362 data. This is most similar to the more challenging Benchmark II. There are a large number
 363 of transition zones, where the type of boundary condition changes, while we still expect a
 364 smooth behaviour of the solution. We were able to achieve a smooth solution and high-
 365 order convergence by using the proposed smoothing approach, and we will use that for
 366 the real application. Further investigations are needed regarding how to choose smoothing
 367 parameters such as the size of the transition zone.

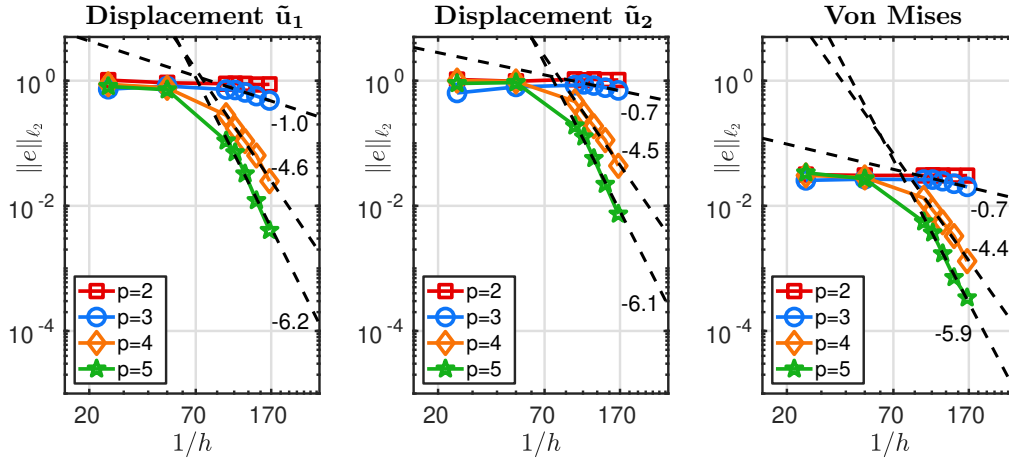


Figure 17: Benchmark II: Convergence of the displacements \tilde{u}_1 and \tilde{u}_2 and the Von Mises stress for different polynomial degrees p , towards a dense numerical reference computed using the unfitted RBF-FD-LS method with $h = 0.002$, $p = 5$.

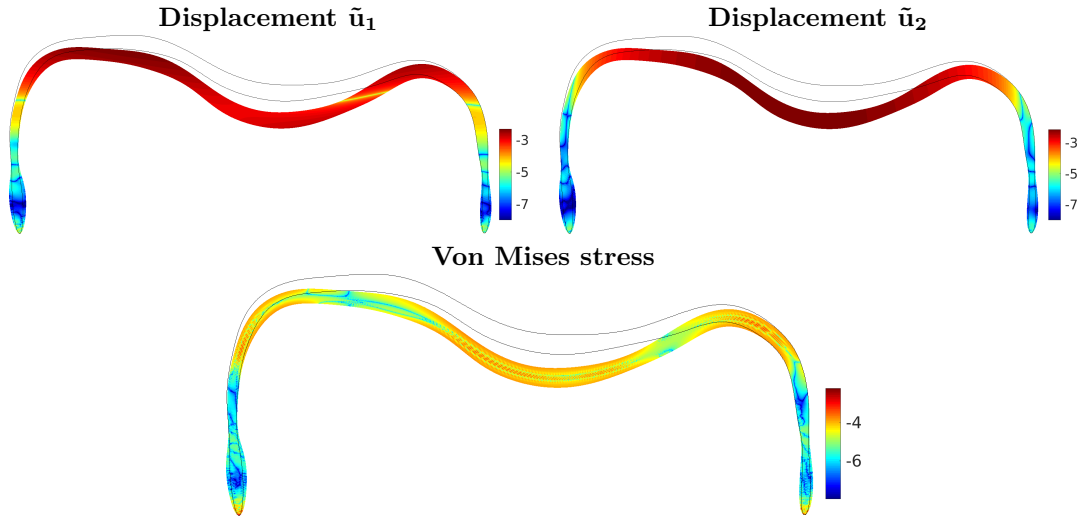


Figure 18: Benchmark II: Error distribution in logarithmic scale for $h = 0.006$ and $p = 5$ when a fine unfitted RBF-FD-LS solution ($h = 0.002$, $p = 5$) is taken as reference for computing the error.

368 To validate the unfitted RBF-FD solver, we measured convergence both against a self
 369 reference and against a highly resolved linear FEM solution. The results show that the two
 370 methods agree to high accuracy.

371 Future work includes employing an unfitted RBF-FD-LS method to solve a more complex
 372 elastic problem, where we are going to use the 3D geometry and forcing data, both extracted
 373 from the CT (computed tomography) images of the diaphragm.

374 **Acknowledgments**

375 The INVIVE project is funded by the Swedish Research Council, grant number 2016-
376 04849.

377 **References**

378 **References**

- 379 [1] WHO, Report of the WHO-China joint mission on Coronavirus disease 2019
380 (COVID-19), [https://www.who.int/docs/default-source/coronaviruse/
381 who-china-joint-mission-on-covid-19-final-report.pdf](https://www.who.int/docs/default-source/coronaviruse/who-china-joint-mission-on-covid-19-final-report.pdf) (February 2020).
- 382 [2] M. Llano-Diez, G. Renaud, M. Andersson, H. Gonzales Marrero, N. Cacciani, H. En-
383 gquist, R. Corpeño, K. Artemenko, J. Bergquist, L. Larsson, Intensive care unit muscle
384 wasting : mechanisms and intervention strategies, *Critical Care* 16:R209 (2012).
- 385 [3] A. A. Kononowicz, N. Zary, S. Edelbring, J. Corral, I. Hege, Virtual patients - what
386 are we talking about? A framework to classify the meanings of the term in healthcare
387 education, *BMC Med. Educ.* 15:11 (2015) 1–7.
- 388 [4] S. Jaber, G. Bellani, et al., The intensive care medicine research agenda for airways,
389 invasive and noninvasive mechanical ventilation, *Intensive Care Med.* 43 (2017) 1352–
390 1365.
- 391 [5] N. Cacciani, E. Larsson, A. Lauro, M. Meggiolaro, A. Scatto, I. Tominec, P.-F. Villard,
392 A first meshless approach to simulation of the elastic behaviour of the diaphragm, in:
393 S. Sherwin, D. Moxey, C. Schwab, J. Peiro, P. Vincent (Eds.), *Spectral and High Order
394 Methods for Partial Differential Equations ICOSAHOM 2018*, Vol. 134 of *Lecture Notes
395 in Computational Science and Engineering*, Springer Nature Switzerland AG, 2020, pp.
396 349–360.
- 397 [6] E. Larsson, P.-F. Villard, I. Tominec, U. Sundin, N. Cacciani, An isogeometric least-
398 squares radial basis function partition of unity method for pdes in thin volumes,
399 Manuscript in preparation, the title and the author list might change (2020).
- 400 [7] I. Tominec, E. Breznik, An unfitted rbf-fd method in a least-squares setting for elliptic
401 pdes on complex geometries (2020). [arXiv:2007.07775](https://arxiv.org/abs/2007.07775).
- 402 [8] I. Tominec, E. Larsson, A. Heryudono, A least squares radial basis function finite
403 difference method with improved stability properties (2020). [arXiv:2003.03132](https://arxiv.org/abs/2003.03132).
- 404 [9] B. Fornberg, N. Flyer, A primer on radial basis functions with applications to the
405 geosciences, Vol. 87 of *CBMS-NSF Regional Conference Series in Applied Mathematics*,
406 Society for Industrial and Applied Mathematics (SIAM), Philadelphia, PA, 2015. [doi:
407 10.1137/1.9781611974041.ch1](https://doi.org/10.1137/1.9781611974041.ch1).
- 408 [10] H. Ladjal, B. Shariat, J. Azencot, M. Beuve, Appropriate biomechanics and kinematics
409 modeling of the respiratory system: Human diaphragm and thorax, in: *2013 IEEE/RSJ
410 International Conference on Intelligent Robots and Systems*, Tokyo, IEEE, 2013, pp.
411 2004–2009.

- 412 [11] H. Ladjal, J. Azencot, M. Beuve, P. Giraud, J. M. Moreau, B. Shariat, Biomechanical
413 modeling of the respiratory system: Human diaphragm and thorax, in: Computational
414 Biomechanics for Medicine, Springer, 2015, pp. 101–115.
- 415 [12] H. Ladjal, N. Skendraoui, M. Giroux, Y. Touileb, J. Azencot, B. Shariat, M. Beuve,
416 P. Giraud, Physiological and biomechanical model of patient specific lung motion based
417 on 4D CT images, in: 2015 8th Biomedical Engineering International Conference (BME-
418 iCON), IEEE, 2015, pp. 1–5.
- 419 [13] M. Giroux, H. Ladjal, M. Beuve, B. Shariat, Biomechanical patient-specific model of the
420 respiratory system based on 4D CT scans and controlled by personalized physiological
421 compliance, in: M. Descoteaux, L. Maier-Hein, A. Franz, P. Jannin, D. L. Collins,
422 S. Duchesne (Eds.), Medical Image Computing and Computer-Assisted Intervention -
423 MICCAI 2017, Springer International Publishing, Cham, 2017, pp. 216–223.
- 424 [14] H. Ladjal, M. Giroux, M. Beuve, P. Giraud, S. Behzad, Patient-specific physiological
425 model of the respiratory system based on inverse finite element analysis: A comparative
426 study, in: 44th Congress of the Société de Biomécanique, Vol. 22 of Computer Methods
427 in Biomechanics and Biomedical Engineering, 2019, pp. S84–S86.
- 428 [15] M. P. Pato, N. J. Santos, P. Areias, E. B. Pires, M. de Carvalho, S. Pinto, D. S. Lopes,
429 Finite element studies of the mechanical behaviour of the diaphragm in normal and
430 pathological cases, *Comput Methods Biomech Biomed Engin* 14 (6) (2011) 505–513.
- 431 [16] B. Fuerst, T. Mansi, F. Carnis, M. Sälzle, J. Zhang, J. Declerck, T. Boettger, J. Bay-
432 outh, N. Navab, A. Kamen, Patient-specific biomechanical model for the prediction of
433 lung motion from 4-D CT images, *IEEE transactions on medical imaging* 34 (2) (2014)
434 599–607.
- 435 [17] P.-F. Villard, P. Boshier, F. Bello, D. Gould, [Virtual Reality Simulation of Liver Biopsy
436 with a Respiratory Component](#), in: H. Takahashi (Ed.), *Liver Biopsy*, InTech, 2011.
437 URL <https://hal.inria.fr/inria-00621263>
- 438 [18] B. Lévy, Y. Liu, Lp centroidal voronoi tessellation and its applications, *ACM Transac-
439 tions on Graphics (TOG)* 29 (4) (2010) 119.
- 440 [19] L. M. Zatz, R. E. Alvarez, An inaccuracy in computed tomography: The energy
441 dependence of ct values, *Radiology* 124 (1) (1977) 91–97, PMID: 866662. doi:
442 [10.1148/124.1.91](https://doi.org/10.1148/124.1.91).
- 443 [20] V. Bayona, N. Flyer, B. Fornberg, G. A. Barnett, On the role of polynomials in RBF-
444 FD approximations: II. Numerical solution of elliptic PDEs, *J. Comput. Phys.* 332
445 (2017) 257–273. doi:[10.1016/j.jcp.2016.12.008](https://doi.org/10.1016/j.jcp.2016.12.008).
- 446 [21] V. Bayona, N. Flyer, B. Fornberg, On the role of polynomials in RBF-FD approxima-
447 tions: III. Behavior near domain boundaries, *J. Comput. Phys.* 380 (2019) 378–399.
448 doi:[10.1016/j.jcp.2018.12.013](https://doi.org/10.1016/j.jcp.2018.12.013).
- 449 [22] V. Bayona, An insight into RBF-FD approximations augmented with polynomials,
450 *Comput. Math. Appl.* 77 (2019) 2337–2353. doi:[/10.1016/j.camwa.2018.12.029](https://doi.org/10.1016/j.camwa.2018.12.029).

- 451 [23] G. A. Barnett, A Robust RBF-FD Formulation based on Polyharmonic Splines and
452 Polynomials, Ph.D. thesis, University of Colorado at Boulder, Dept. of Applied Math-
453 ematics, Boulder, CO, USA (2015).
- 454 [24] I. Tominec, Rectangular and square RBF-FD matrices in MATLAB, [https://github.
455 com/IgorTo/rbf-fd](https://github.com/IgorTo/rbf-fd) (2021). doi:10.5281/zenodo.4525550.
- 456 [25] C. Geuzaine, GetDP: a general finite-element solver for the de Rham complex, in:
457 PAMM Volume 7 Issue 1. Special Issue: Sixth International Congress on Industrial
458 Applied Mathematics (ICIAM07) and GAMM Annual Meeting, Zürich 2007, Vol. 7,
459 Wiley, 2008, pp. 1010603–1010604.